Thermofluid Design and Performance Evaluation of a Natural Draft Air-Cooled Condenser Towards Annual Performance Modelling of Concentrated Solar Power Plants

Tristan Nel , Johannes P Pretorius * , Pieter G Rousseau

Posted Date: 3 June 2026

doi: 10.20944/preprints202606.0307.v1

Keywords: natural draft air-cooled condenser; dry cooling; 1-D thermofluid model; optimisation; computational fluid dynamics; surrogate model; annual performance modelling methodology; concentrated solar power

 doi:10.20944/preprints202606.0307.v1

Article

Thermofluid Design and Performance Evaluation of a Natural Draft Air-Cooled Condenser Towards Annual Performance Modelling of Concentrated Solar Power Plants

Tristan Nel, Johannes P Pretorius * and Pieter G Rousseau

Department of Mechanical and Mechatronic Engineering, Stellenbosch University, Cnr Joubert and Banghoek Road, Stellenbosch, 7600, South Africa

* Correspondence: jpp@sun.ac.za

Abstract

This paper presents the sizing and performance evaluation of a natural draft air-cooled condenser with nominal heat rejection capacity of 75 MW_{th} for implementation at a concentrated solar power plant in the Northern Cape province, South Africa. Initial sizing and optimisation of the tower geometry is done with the aid of a one-dimensional thermofluid model at design conditions. An exhaustive search optimisation is used based on Latin hypercube sampling that covers the geometric design envelope, which is defined via the tower and heat exchanger heights, and the tower base and outlet diameters. Following this, the performance of the best-performing tower geometry is verified via detailed three-dimensional computational fluid dynamics (CFD), and the geometry adjusted slightly to achieve the desired heat rejection capacity. This process includes validation of the CFD model against previous work as well as performing grid convergence studies to ensure mesh independence. Finally, a methodology is presented to evaluate the performance of the system over the full range of ambient conditions encountered during an annual operating cycle. The methodology will be applied in further work to develop a reduced order surrogate model for application in annual performance studies.

Keywords: natural draft air-cooled condenser; dry cooling; 1-D thermofluid model; optimisation; computational fluid dynamics; surrogate model; annual performance modelling methodology; concentrated solar power

1. Introduction

South Africa, among many other countries, continues to experience an increase in demand for electricity generation. This is both due to an increased population and the booming field of Artificial Intelligence (AI) [1,2]. At the same time, sustainability concerns require the energy sector to look for more "green" alternatives [3]. South Africa has the advantage of high solar density [4], making concentrated solar power (CSP) plants a relatively attractive solution. However, the water consumption demands of high efficiency wet cooling systems preclude their use in this semi-arid region, with modern plants instead employing dry cooling as the standard [5,6].

Conventional dry cooling systems consist mainly of two possibilities: indirect natural draft systems and direct forced draft systems. Direct systems, or air-cooled condenser (ACC) systems, exhibit lower capital costs but require a large parasitic load to power the fans. Additionally, the system requires more regular maintenance due to its large number of moving parts. Indirect systems need greater capital investments, but parasitic loads from their associated pumps are much reduced compared to that of the ACC's multitude of fans. Indirect systems, however, exhibit reduced thermal efficiency due to additional intermediate heat exchange stages to reject the heat of the cycle from the

 doi:10.20944/preprints202606.0307.v1

working fluid to the ambient environment [7]. Numerous studies have been conducted on the performance prediction of these systems under design and off-design conditions [8–11]. These investigations typically consider simulated performance under varying ambient conditions, especially the effects of wind. Wind is of particular interest due to its negative impact on system performance.

A modern competitive alternative to these systems, which has garnered some attention from researchers recently, is the natural draft direct dry cooling system (NDDDCS), which, when condensing the working fluid, is simply referred to as the natural draft air-cooled condenser (NDACC). The direct heat rejection configuration of this system allows high thermal efficiency and corresponding reduced capital costs compared to the indirect system. In addition, with no fans or pumps, parasitic power consumption and associated maintenance costs are eliminated.

The NDACC was first simulated by Kong et al. [12] for large-scale applications (~1000 MW_{th}). Like other dry cooling systems, the wind influences NDACC performance. To mitigate wind effects, the optimal arrangement of heat exchangers within the system was investigated. Kong et al. [12,13] determined whether vertically arranged heat exchangers, horizontally arranged heat exchangers or a combination of the two lead to increased cooling efficiency. It was ultimately found that vertically arranged heat exchangers are the most effective. Kong et al. [14] go on to investigate the angle between the delta-shaped heat exchanger bundles that minimize the impact of wind. Vertical heat exchangers with an angle of 150° was shown to be the most robust with respect to performance degradation from wind. Additionally, their further work [15] explored the effect of radial wind walls to improve performance during strong winds and found that equally spaced walls with one wall at each heat exchanger apex provide the lowest decrease in performance due to wind.

Strydom et al. [16] goes on to model the NDACC at several different application scales, including a “medium sized” tower for CSP application. This was done with both a one-dimensional (1-D) model [17,18] and three-dimensional (3-D) computation fluid dynamics (CFD) simulations [19]. The 1-D model focussed on predicting the heat rejection and mass flow rate of air through the cooling tower at design conditions. It employs a heat transfer resistance network developed from the work of Kröger [20]. The CFD simulations build on the work by Kong et al. [12], incorporating improved atmospheric modelling and opting for a porous zone formulation to model the heat exchangers instead of a radiator model. All CFD simulations were conducted with vertical heat exchangers employing an apex angle of 60°, and similar trends heat rejection deterioration under wind were observed compared to previous work (~50% under a worst-case scenario). It was noted that smaller systems were more sensitive to wind, experiencing similar performance deterioration at lower wind speeds compared to larger systems.

This however is not reflective of the true cooling tower behaviour when integrated with the turbine. When the ambient conditions change such that heat rejection decreases, the integrated system responds by increasing the back pressure. This results in a minimal decrease in true heat rejection with an associated decrease in turbine efficiency [21].

This paper forms part of a project where the back pressure response associated with an NDACC with nominal heat rejection capacity of 75 MW_{th} will be coupled with a steam turbine model to predict the annual integrated performance of a CSP power plant in Upington, in the Northern Cape province of South Africa.

The paper will focus on three aspects. The first is the design and sizing methodology to obtain the optimum NDACC tower geometry using a 1-D thermofluid model, similar to that developed by Strydom [16]. While the modelling approach is mainly based on prior work, this study presents, for the first time, the resulting optimised NDACC geometry for a 50 MWe CSP application, determined through an integrated cost and performance evaluation. The second aspect is the development and validation of a CFD model of the optimum geometry. This process includes validation of the CFD model against previous work as well as performing convergence studies to ensure mesh independence. Several enhancements are introduced to improve both model accuracy and computational efficiency, most notably the contribution of a higher-accuracy representation of the heat exchanger within the porous zone formulation. Finally, the paper presents a methodology that can be applied to evaluate the performance of the tower over the full range of ambient conditions

 doi:10.20944/preprints202606.0307.v1

encountered during an annual operating cycle. The results of this will serve as training data for a surrogate model that can be coupled with a turbine model to predict the integrated annual performance of the CSP plant. This approach draws on works similar to Haffajee et al. [22], while extending the application from real-time monitoring to annual performance evaluation. To the authors' knowledge, this is the first framework of its kind for predicting the integrated annual performance of a coupled turbine-NDACC system.

2. Materials and Methods

The NDACC system employs similar geometric features to indirect natural draft dry cooling systems. This allows the tower design to be modelled according to dimensions defined by Kröger [20] for an indirect cooling tower, as shown in Figure 1. In this schematic H_5 refers to the total tower height, H_4 to the heat exchanger height, d_5 to the outlet diameter, and d_3 to the base diameter. Additionally, to keep the design consistent with previous work, it was assumed that the tower diameter remains constant above the throat height. The throat height, H_t, refers to the height above ground level at which the tower diameter reaches a minimum. Throat height was taken to be 91.1% of the total tower height, as was done in previous work.

Another aspect of the tower geometry to consider is the heat exchanger configuration. For this paper it is assumed that the tower has vertically arranged heat exchanger banks, as Kong et al. [12] noted that this results in superior performance compared to horizontal heat exchangers. These banks feature a typical delta heat exchanger arrangement, with 60° apex angle. This study uses the same heat exchanger finned tubes as in Strydom et al. [16]. For the specific dimensions of the finned tubes please refer to Table 1 and Figure 2.

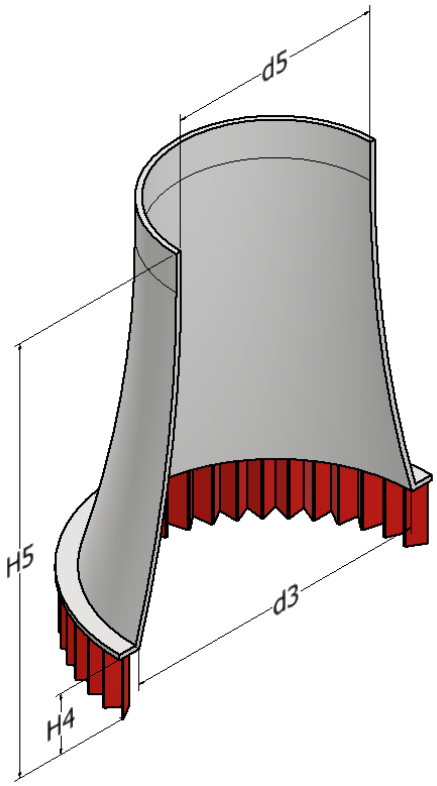

Figure 1. Schematic section of NDACC geometry with reference dimensions.

 doi:10.20944/preprints202606.0307.v1

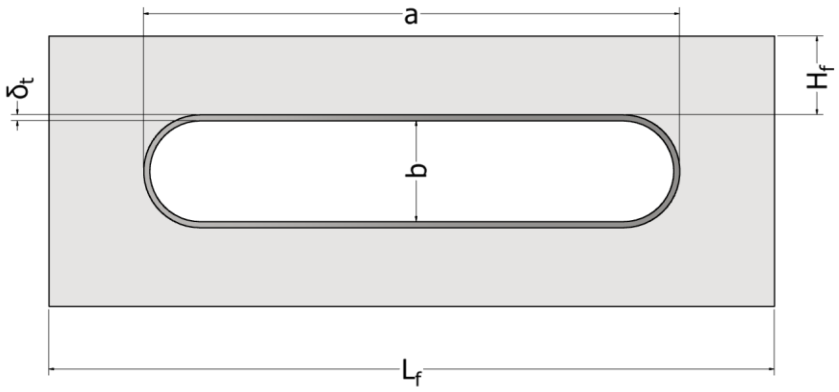

Figure 2. Cross-section schematic of finned tube with major dimensions.

Table 1. Finned tube dimensions.

Description	Symbol	Value (m)
Major tube axis	a	0.13
Minor tube axis	b	0.025
Tube wall thickness	δ_t	0.0015
Tube pitch	p_t	0.067
Fin length	L_f	0.18
Fin width	H_f	0.0195
Fin thickness	δ_f	0.00025
Fin pitch	p_f	0.0023

The Northern Cape region in South Africa receives some of the highest solar irradiation globally [23] and as a result several utility-scale commercial solar power plants have been constructed in the area. The CSP power plant under consideration will be located in Upington in the Northern Cape province, and requires an NDACC with a nominal heat rejection capacity of 75 MW_{th} at the design operating conditions.

A suitable design point should be selected for the NDACC, which governs its relative sizing. For CSP plants employing dry cooling systems, the design point is typically selected at ambient temperatures higher than the annual mean to ensure a relatively large cooling system capacity, thereby minimizing the extent to which the cooling system further constrains the achievable power plant output. Using historical meteorological data at Upington between 2017 and 2022, the NDACC design point was selected as 10 kPa(a) back pressure at an ambient temperature of 28 °C. The selected design point results in an initial temperature difference (ITD) of approximately 17.8 °C, which compares well with the ITDs of other operating dry cooling systems in the area.

2.1. One-Dimensional Model

The 1-D steady-state NDACC model developed in this work is similar to that of Strydom et al. [17], who utilises numbering conventions and builds on theory from Kröger [20]. The governing equations presented in the following section are similar to previous work and is repeated here for completeness. After validation of the model (refer to section 3.1.1), the solution algorithm is modified to allow for the calculation of a best-performing NDACC configuration within specified constraints. The details hereof are discussed in Section 2.1.2.

2.1.1. Governing Equations

The 1-D model calculates the thermofluid performance of a fixed geometry NDACC by simultaneously solving the governing energy and momentum balance equations on the steam and air sides. The steam-side momentum balance represents the pressure drop of the steam from the turbine exhaust to the mean pressure in the heat exchanger bundles. This pressure drop is calculated

 doi:10.20944/preprints202606.0307.v1

in two components, one from the turbine exhaust to the inlet header of the heat exchanger, and another from the header to the mean pressure in the finned tubes, as follows:

$$p_{v1} - p_{v2} = \frac{1}{2}(K_{v2} + K_{sd})\rho_{v2}v_{v2}^2 \quad (1$$

where p_{v2}, ρ_{v2} and v_{v2} are the pressure, density and velocity of the steam at the header inlet respectively, while p_{v1} is the pressure at the turbine exhaust. K_{v2} is the coefficient related to the contraction losses at the inlet header and K_{sd} is the coefficient for the losses in the steam duct, assumed to be a constant value of 2.5 [20]. The coefficient for the contraction losses can be calculated as follows:

$$K_{v2} = 1 - \left(\frac{W_t L_t n_{tb} n_b}{A_{fr}}\right)^2 + K_C \quad (2$$

In this equation, K_C refers to a loss coefficient associated with the inlet header, and it is assumed to have a value of 0.6 [20]. Additionally, W_t and L_t refer to the inner finned tube with (minor axis) and finned tube length, respectively. A_{fr}, n_{tb} and n_b designate the total frontal area of the heat exchangers, tubes per heat exchanger bundle and the total number of bundles. The second pressure drop component from the header inlet to the mean tube pressure can be calculated from:

$$p_{vm} = p_{v2} - \frac{0.1582\mu_{v2}^2 L_t}{\rho_{v2} d_e^3 Re_{v2}}(0.267a_1 Re_{v2}^{2.75} + 0.364a_2 Re_{v2}^{1.75}) + \frac{2}{3}\rho_{v2}v_{v2}^2 \quad (3$$

$$a_1 = 1.0649 + 1.041(10^{-3})Re_{vn} - 2.011(10^{-7})Re_{vn}^3 \quad (4$$

$$a_2 = 290.1479 + 59.3153Re_{vn} + 1.5595(10^{-2})Re_{vn}^3 \quad (5$$

$$Re_{vn} = Re_{v2}\frac{W_t}{2L_t} \quad (6$$

where p_{vm} refers to the mean pressure within the heat exchanger tubes, μ_{v2} refers to the dynamic viscosity of the steam at the header inlet, d_e is the hydraulic diameter of the tubes and Re is the Reynolds number of the fluid.

The model assumes that the steam within the NDACC is at saturated conditions. Kröger [20] provides the following empirical correlation for calculating the saturated steam temperature from a given saturated steam pressure. Equation (7) shows the case where this correlation is used to calculate the saturation steam temperature at the inlet to the tubes, but it can equally be used to calculate the temperature from the mean tube pressure.

$$T_{v2} = \frac{5149.6889682}{\ln\left(\frac{1.020472843 * 10^{11}}{p_{v2}}\right)} \quad (7$$

With the mean steam temperature found within the heat exchanger tubes, an energy balance can be performed across the heat exchangers, as follows:

$$\dot{Q} = \dot{m}_a c_{pa}(T_{a3} - T_{a2}) = \dot{m}_a c_{pa}\epsilon\,(T_{vm} - T_{a2}) = \dot{m}_c h_{fg} \quad (8$$

where T_{a3} is the air temperature directly after the heat exchanger, T_{a2} is the air temperature just before the heat exchanger (at half of the height exchanger height), T_{vm} is the mean temperature of the steam in the heat exchanger tubes, ϵ is the effectiveness of the heat exchanger, $\dot{Q}$ is the heat rejection rate, $\dot{m}_a$ is the air mass flow rate, c_{pa} is the specific heat capacity of air, $\dot{m}_c$ is the mass flow rate of condensate and h_{fg} is the latent heat vaporisation. The effectiveness uses the standard $\epsilon - NTU$ approach and is given by the pair of equations below:

$$\epsilon = 1 - \exp\left(-\frac{UA}{\dot{m}_a c_{pa}}\right) \quad (9$$

 doi:10.20944/preprints202606.0307.v1

$$UA = \left(\frac{1}{h_{ea}A_a} + \frac{1}{h_c A_c}\right)^{-1} \quad (10$$

where UA is the overall heat transfer coefficient, h_c is the condensation heat transfer coefficient, A_c is the wetted area inside all the heat exchanger tubes upon which condensation occurs. $h_{ea}A_a$ is the effective air side heat transfer conductance, which is given by:

$$h_{ea}A_a = k_a Pr_a^{1/3} A_{fr} N_y \quad (11$$

$$R_y = \frac{\dot{m}_a}{\mu_a A_{fr}} \quad (12$$

$$N_y = 366.007945\, R_y^{0.433256} + 360.588007\, R_y^{0.47037} \quad (13$$

where k_a, μ_a and Pr_a respectively refer to the thermal conductivity, dynamic viscosity and Prandtl number of air. Equation (13) defines the heat transfer performance of the finned tubes. R_y and N_y are the characteristic flow and heat transfer parameters as defined in [20]. The condensation heat transfer coefficient is calculated from:

$$h_c = 0.9245 \left[\frac{k_c^3 \rho_c^2 g h_{fg} H_4}{\mu_c \dot{m}_{ai} c_{pa} (T_{vm} - T_{a2}) \left[1 - exp\left(\frac{-UdzH}{\dot{m}_{ai} c_{pa}}\right)\right]}\right]^{\frac{1}{3}} \quad (14$$

$$\dot{m}_{ai} = \frac{\dot{m}_a}{2 n_{tb} n_b} \quad (15$$

$$UdzH = \frac{h_{ea}A_a}{2 n_{tb} n_b} \quad (16$$

where k_c, ρ_c and μ_c respectively refer to the thermal conductivity, density and dynamic viscosity of the condensate and T_{vm} is the mean steam temperature in the tubes. The condensate formation is approximated by assuming the tube acts as two parallel flat plates, where $\dot{m}_{ai}$ and $UdzH$ are the air mass flow rate and universal heat transfer coefficient for each of these plates.

The final part of the 1-D model is the momentum balance of the air as it flows through the tower, which Kröger [20] simplifies to a so-called draft equation. This equation assumes a dry adiabatic lapse rate in the atmosphere and internally over the height of the tower. The left-hand-side (LHS) of the draft equation represents the draft driving potential, due to buoyancy differences between the column of hot air in the tower and a column of colder air external to the tower, and is shown as Equation (17). This is balanced on the right-hand-side (RHS) by several flow resistance losses as the air flows through the tower, as per Equation (18). For the sake of readability, the draft equation was split into a LHS and RHS below:

$$LHS = p_{a1}\left[\left(1 - 0.00975\frac{H_4}{2T_{a1}}\right)^{3.5}\left(1 - 0.00975\frac{H_5 - \frac{H_4}{2}}{T_{a3}}\right)^{3.5} - \left(1 - 0.00975\frac{H_5}{T_{a1}}\right)^{3.5}\right] \quad (17$$

$$RHS = (K_{il} + K_{he\theta} + K_{ts} + K_{ct})_{he}\left(\frac{\dot{m}_a}{A_{fr}}\right)^2\left(\frac{1}{2\rho_{a23}}\right)\left(1 - 0.00975\frac{H_5 - \frac{H_4}{2}}{T_{a3}}\right)^{3.5} + (K_{to} + a_{e5})\left(\frac{\dot{m}_a}{A_5}\right)^2\left(\frac{1}{2\rho_{a5}}\right) \quad (18$$

where p_{a1} and T_{a1} refer to the atmospheric pressure and temperature at ground level, while ρ_{a23} designates the mean air density through the heat exchanger. ρ_{a5} refers to the density of the air as it exits the tower. The K terms refer to pressure loss coefficients through the tower: K_{il} is the loss through the inlet louvres and is assumed to be a constant of 2.5, $K_{he\theta}$ is the loss across the heat

 doi:10.20944/preprints202606.0307.v1

exchanger, K_{ts} is the loss due to tower supports, K_{ct} is the loss due to redirection and contraction as the air enters the tower, and K_{to} is the tower outlet loss. Each of these, including the velocity correction factor at the tower outlet, a_{e5}, is calculated according to the following set of equations.

$$K_{he} = 4177.08481\, R_y^{-0.4392686} \tag{19}$$

Equation (19) provides an expression for the pressure drop across the heat exchanger for air flowing straight through it. To accommodate redirection, contraction and downstream effects as the air flows through the delta heat exchanger, the equation is adapted to:

$$K_{he\theta} = K_{he} + \frac{2\rho_{a3}}{\rho_{a2}+\rho_{a3}}\left(\frac{1}{\sin(\theta_m)}-1\right)\left[\left(\frac{1}{2\sin(\theta_m)}-1\right)+2K_{ci}^{0.5}\right]+\frac{2\rho_{a3}K_d}{\rho_{a2}+\rho_{a3}} \tag{20}$$

where ρ_{a2} and ρ_{a3} refer to the air density just before and after the heat exchanger. θ_m refers to the mean incidence angle and it is calculated from θ, which is half the apex angle of the heat exchanger (in degrees):

$$\theta_m = 0.0019\,\theta^2 + 0.9133\,\theta - 3.1558 \tag{21}$$

The loss K_d refers to the downstream loss caused by the low-velocity wake from the exhaust angle of the heat exchangers. It is calculated as follows:

$$K_d = \exp\left[5.488405 - 0.21312090\theta + 3.533265(10^{-3})\theta^2 - 0.2901016(10^{-4})\theta^3\right] \tag{22}$$

K_{ci} refers to the entrance contraction loss of the heat exchanger and it can be calculated from the contraction loss, K_c, and the free stream area ratio, σ_{21}. The free stream area ratio is effectively a measure of the porosity of the heat exchanger, calculated from the volume of the finned tubes, V_{he}, and the total volume, V_t. The set of equations for this are given as:

$$K_{ci} = \frac{K_c}{\sigma_{21}^2} \tag{23}$$

$$\sigma_{21} = 1 - \frac{V_{he}}{V_t} \tag{24}$$

$$K_c = \left(1-\frac{1}{\sigma_c}\right)^2 \tag{25}$$

$$\sigma_c = 0.61144517 + 0.0456493\,\sigma_{21} - 0.33651\,\sigma_{21}^2 + 0.4082743\,\sigma_{21}^3 + 2.672041\,\sigma_{21}^4 - 5.963169\,\sigma_{21}^5 + 3.558944\,\sigma_{21}^6 \tag{26}$$

where σ_c refers to the contraction ratio. The tower support and redirection losses are referred to the heat exchanger conditions using density ratios (for the sake of elegant inclusion into the draft equation), and defined as follows:

$$K_{tshe} = \frac{C_{Dts}L_{ts}d_{ts}n_{ts}A_{fr}^2}{(\pi d_3 H_4)^3}\left(\frac{\rho_{a23}}{\rho_{a1}}\right) \tag{27}$$

$$K_{cthe} = \left[2.21 - 0.42\left(\frac{d_3}{H_4}\right)+0.091\left(\frac{d_3}{H_4}\right)^2\right]\left(\frac{A_{e2}}{A_2}\right)^2\left(\frac{\rho_{a23}}{\rho_{a2}}\right) \tag{28}$$

where C_{Dts}, L_{ts}, d_{ts} and n_{ts} is the drag coefficient, length, diameter and number of tower supports. A_{e2} is the total projected frontal area of the heat exchangers and A_2 is the peripheral area of the tower. ρ_{a1} refers to the atmospheric air density at ground level. The tower outlet loss can be found from:

$$K_{to} = -0.129\left(Fr_D\frac{d_5}{d_3}\right)^{-1} + 0.0144\left(Fr_D\frac{d_5}{d_3}\right)^{-1.5} \tag{29}$$

$$a_{e5} = 1.004 + 5.8\left(\frac{d_5}{d_3}\right)^9 + \left[0.007 + 0.043\left(\frac{d_5}{d_3}\right)^{2.5}\right]Fr_D^{-1.5} \tag{30}$$

 doi:10.20944/preprints202606.0307.v1

where Fr_D refers to the Froude number. Froude number can be an indicator of cold inflow and can be calculated as follows:

$$Fr_D = \frac{\left(\frac{\dot{m}_a}{A_5}\right)^2}{[\rho_{a5}(\rho_{a6} - \rho_{a5})g d_5]} \quad (31$$

where A_5 is the outlet area of the tower, ρ_{a5} refers to the density of the heated air at the tower outlet and ρ_{a6} refers to the density of the ambient air at the tower outlet height. With these equations the heat rejected can be calculated for a given tower geometry by simultaneously solving the two momentum and three energy balance equations.

2.1.2. Sizing Methodology

The 1-D model produced by Strydom [16] can analyse the tower given any reference dimensions as described in Figure 1. In this work however, some model modifications were made to improve performance prediction accuracy, while also changing the required output from heat rejection to geometric designs. One major modification involved updating the calculation of heat exchanger width so that realistic bundle geometries are modelled, given their placement in delta configuration around the circumference of the tower. Through careful trigonometric analysis, the following set of equations allow calculation of an accurate bundle width (see Figure 3):

$$W_b = \frac{S - \Delta S}{\cos(\beta)} \quad (32$$

$$S = \frac{d_3}{2}\tan\left(\frac{360}{n_b}\right) \quad (33$$

$$\Delta S = \frac{L_f}{\sin(\alpha_1)}\sin(\alpha_2) \quad (34$$

$$\beta = 90 - \theta \quad (35$$

$$\alpha_1 = 90 + \frac{360}{n_b} \quad (36$$

$$\alpha_2 = 90 - \alpha_1 + \beta \quad (37$$

 doi:10.20944/preprints202606.0307.v1

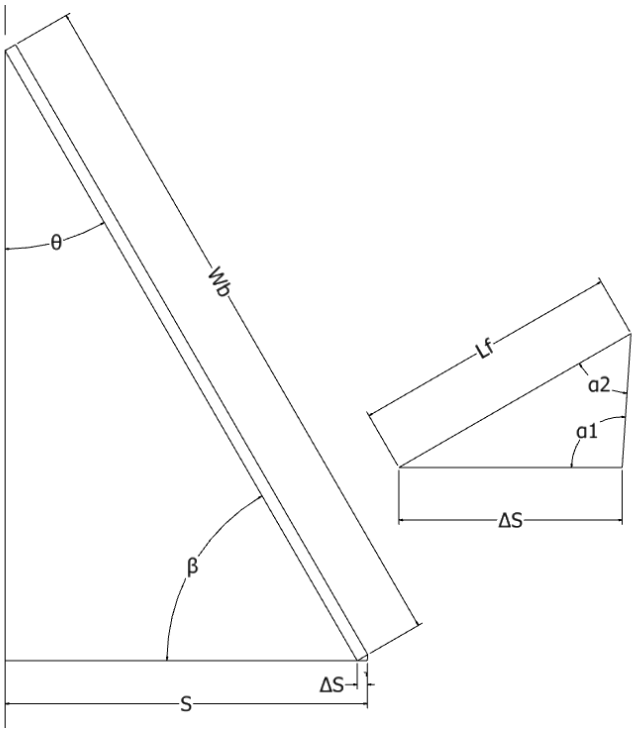

Figure 3. Heat exchanger width formulation.

As noted above, in this work the purpose of the 1-D model is modified to predict the four dimensions given in Figure 1, such that their implementation in the performance calculation produces a required heat rejection rate. This introduces complexity however, since several sets of dimensions could match a single heat rejection rate. To remedy this an exhaustive search was employed and the search space was modified such that the parameters of the search space do not directly influence the tower size. This was achieved by selecting three geometric ratios as defined in [20]:

$$r_1 = \frac{H_5}{d_3}, \qquad (1.0 < r_1 < 1.4) \tag{38}$$

$$r_2 = \frac{d_5}{d_3}, \qquad (0.5 < r_2 < 0.7) \tag{39}$$

$$r_3 = \frac{d_5}{H_4}, \qquad (5 < r_3 < 15) \tag{40}$$

Note that the ranges provided with Equations (38)–(40) are ratios of existing cooling towers and are physically feasible values. By using these ratios all four dimensions of the tower become related and thus a single scaling factor can be used to match the requested heat rejection rate for a given set of ratios and ambient conditions. This involves the iterative solution of the two momentum balance equations and three energy balance equations, yielding: the mass flow rate of steam, the mass flow rate of the air, the average temperature of the heat exchanger wall and the temperature of the air directly behind the heat exchanger.

An exhaustive search that employs Latin hypercube sampling (LHS) was applied to generate different sets of feasible geometric ratios. For each of these geometric ratio sets, a tower height is first guessed and the heat rejected is predicted for that tower height. If this prediction is above the target heat rejection, the tower height is decreased and if the prediction is lower than the target heat rejection, the tower height is increased. The result of this process is a dataset with a number of rows equal to the sample size and each row containing the three geometric ratios and the tower height required to match the target heat rejection. A flow diagram depicting this methodology is shown in Figure 4.

 doi:10.20944/preprints202606.0307.v1

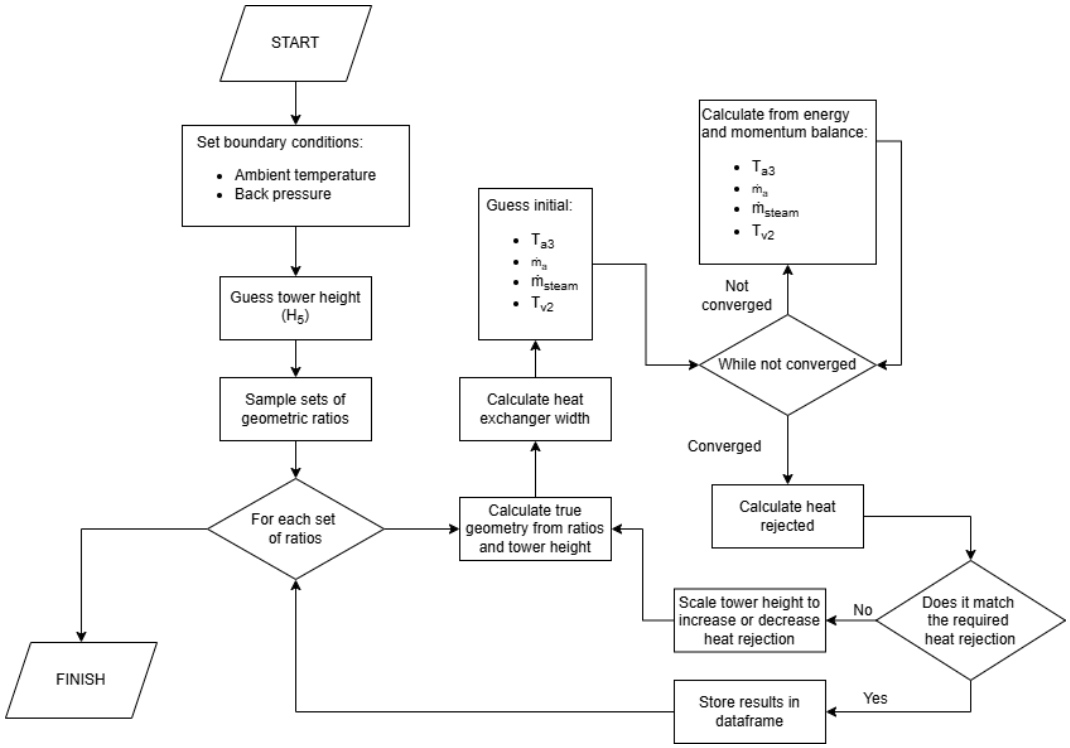

Figure 4. Sizing methodology.

From the dimensions of each modelled NDACC alternative, an associated system material cost can be calculated based on the volume of each material. It should be noted that for the sizing it was assumed all towers have a constant wall thickness of 0.5 m. The heat exchangers are assumed to be manufactured from AISI 304 stainless steel (3.08 USD/kg) for the tubes and aluminium (4.62 USD/kg) for the fins. The tower geometry is made from rebar reinforced concrete (277.12 USD/m^3). This was then repeated for various sets of geometric ratios until a four-dimensional space was created with the three ratios and material cost. From this a minimised cost was selected, yielding the best-performing geometric ratios. In this way the authors were able to identify the most cost-effective NDACC system geometry that achieves the target heat rejection rate at the lowest material cost. The reader is referred to section 3.1.2 for the results of this methodology.

2.2. CFD Model

Once the best-performing ratios for the NDACC were obtained using the 1-D model, the geometry was created in ANSYS SpaceClaim, meshed in ANSYS Mechanical and simulated in ANSYS Fluent 2024 R2. Due to inherent differences in the prediction accuracies between 1-D and 3-D CFD models [16], minor modifications to the best-performing NDACC dimensions were necessary to ensure that the required performance was met. This was performed iteratively until the required heat rejected was matched. The reader is referred to section 3.2.2 for the results of this sizing. It should also be noted that a constant tower shell and clapboard thickness of 0.5 m is employed in the CFD model.

Work by [24] has shown that steady-state CFD simulation results are virtually identical when modelling using full or half cylinder domains for natural draft direct dry cooling systems. Therefore, to save on computational cost, and due to the application of symmetric boundary conditions in this work, a half cylinder domain is employed. It contains half the cooling tower with a total height of at least 6 times that of the tower being simulated and a diameter of at least 24 times that of the tower. See Figure 5 for reference:

 doi:10.20944/preprints202606.0307.v1

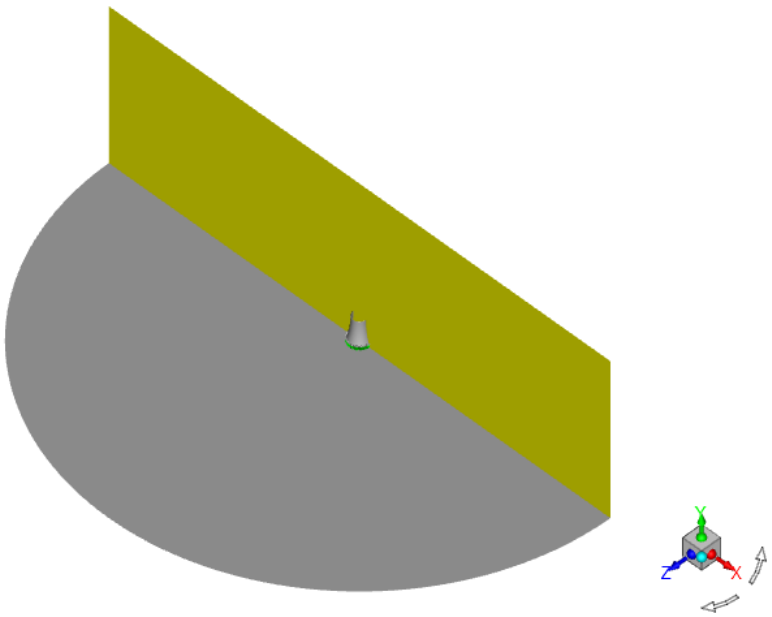

Figure 5. CFD domain.

2.2.1. Numerical Modelling

The 3-D steady-state CFD model developed in this work solves the governing equations listed in Table 2. These equations assume steady compressible flow, excluding the viscous stresses [25].

Table 2. Transport equations.

Description	Equation
Continuity	$\nabla(\rho\vec{u}) = 0$
X-momentum	$\nabla(\rho u\vec{u}) = \frac{\partial p}{\partial x} + \nabla[(\mu + \mu_t)\nabla(u)] + S_{Mx}$
Y-momentum	$\nabla(\rho v\vec{u}) = \frac{\partial p}{\partial y} + \nabla[(\mu + \mu_t)\nabla(v)] + S_{My}$
Z-momentum	$\nabla(\rho w\vec{u}) = \frac{\partial p}{\partial z} + \nabla[(\mu + \mu_t)\nabla(w)] + S_{Mz}$
Energy	$\nabla(\rho i\vec{u}) = -p\nabla(\vec{u}) + \nabla[k\nabla(T)] + \phi + S_i$

In these transport equations $\vec{u}$ refers to the velocity vector with x-component u, y-component v and z-component w. μ refers to the dynamic viscosity of the fluid and μ_t is an additional component added to the dynamic viscosity to capture turbulent behaviour. The source terms in the equations are denoted by S. The pressure is referred to as p and temperature as T. The density is given by ρ and the thermal conductivity is k.

The $k-\omega$ SST turbulence model with default enhanced wall treatment option was selected for the simulation, as it has been shown to have a relatively high accuracy near walls regardless of the refinement level of the mesh near walls [26]. It should be noted that this does not mean accuracy cannot be improved by a finer mesh but for a coarse mesh a higher accuracy is achieved. Additionally, this model has shown itself capable of predicting flow separation well [27]. The only drawback of this model is the fact that it does not accurately predict true turbulent behaviour, so the model cannot predict true plume dissipation, but that is beyond the scope of this study.

To solve the pressure-velocity coupling, the SIMPLE algorithm was used. This approach was preferred over SIMPLEC, as it provides a more robust solution, and over PISO, as the model aims to predict an average heat rejection at steady-state rather than a true transient simulation [28].

Since the cooling tower is driven by hydrostatic forces, PRESTO! was used as the pressure interpolation scheme. All other schemes were selected as second-order upwind differencing schemes. Air was assumed to be an ideal gas, with correlations for thermal conductivity, specific heat capacity and viscosity based on temperature only, from [20].

 doi:10.20944/preprints202606.0307.v1

Each simulation was run with the under-relaxation factors shown in Table 3 until the convergence criteria in Table 4 was met and the heat rejection value converged.

Table 3. Under-relaxation factors.

Relaxation Factor	Value
Pressure	0.2
Density	0.9
Body forces	0.9
Momentum	0.5
Turbulent kinetic energy	0.75
Turbulent dissipation rate	0.75
Turbulent viscosity	0.5
Energy	0.9

Table 4. Convergence criteria.

Description	Accuracy
Continuity	1e-4
Velocity	5e-6
Turbulent kinetic energy	5e-3
Turbulent dissipation rate	5e-4
Energy	1e-6

2.2.2. Boundary Conditions

The results of the CFD are directly correlated with the boundary conditions applied and thus it is crucial that the pressure, temperature and wind profile at the boundaries are modelled with sufficient accuracy.

The atmospheric pressure gradient can be adopted from the 1-D model with minor changes. The temperature gradient, however, cannot be incorporated properly due to the manner in which Fluent solves buoyancy problems. If both the temperature and pressure gradient were implemented the temperature difference correlates to a density difference and thus a buoyancy force drives movement leading to instability, as the domain becomes hydrostatically unstable. This implies that the CFD model does not capture the dry adiabatic lapse rate and instead assumes an isothermal atmosphere. This was deemed acceptable as both Kong et al. [12] and Strydom et al. [19] modelled the tower accurately despite this limitation. The modified atmospheric pressure gradient is therefore derived from Equation (41), assuming constant temperature, which yields Equation (42):

$$\frac{dp}{dy} = -\frac{pM_a g}{RT} \tag{41}$$

$$p_{y2} = p_{y1} e^{-\frac{ygM_a}{RT}} \tag{42}$$

where y is the vertical height above ground level. M_a, g and R refer to the molecular mass of air, gravitational acceleration, the universal gas constant respectively. In Equation (42), p_{y2} is the pressure at the height being evaluated, while p_{y1} refers to the pressure at ground level.

Unlike the 1-D model, the CFD model is capable of modelling crosswind. It does this through a logarithmic implementation of the wind velocity profile. A reference wind speed (v_{ref}) is taken at 10 m above ground level and then fitted to the following logarithmic profile employed by both Kong et al. [15] and Kröger [20], with an exponent of 0.2:

$$v_{cw} = v_{ref} \left(\frac{y}{10}\right)^{0.2} \tag{43}$$

where v_{cw} is the wind velocity at the evaluation height and v_{ref} is the velocity at the reference point of 10 m above ground level.

 doi:10.20944/preprints202606.0307.v1

Additionally, the turbulence intensity and viscosity ratio were set to 0.1% and 0.1 respectively, as was done by Kong et al. [15]. All walls were taken to be adiabatic with a no slip condition (this includes the ground and tower shell).

For the no-wind scenario, the domain inlets (Figure 6, circumferential blue and red planes) are defined as pressure inlet boundaries, while the upper boundary of the domain (Figure 6, top red plane) is specified as a pressure outlet. In the crosswind scenario, a velocity inlet boundary condition is applied at the inlet (Figure 6, circumferential blue plane), with the outlet boundaries defined as pressure outlets (Figure 5, circumferential and top red planes). The velocity-inlet specified both Equations (42) and (43) for the pressure and velocity profile respectively. Note that the velocity component is set such that the crosswind is parallel and upwind of the tower. Only Equation (42) was specified for both pressure-outlets. To assist simulation stability, the pressure-outlet at the top of the domain was set to prevent back-flow. The remaining boundary was set to a symmetry plane (Figure 5, yellow).

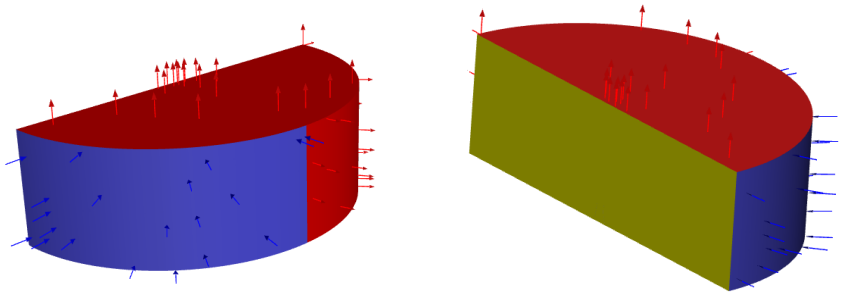

Figure 6. Boundary conditions.

2.2.3. Heat Exchanger Model

To model the heat rejection of the NDACC, two modelling approaches were implemented. The first approach replicated the methodology reported by Strydom et al. [16] and was used solely for validation purposes. Although the use of one model for validation and another for predictive analysis may appear counterintuitive, this strategy was necessary to ensure that the computational domain and boundary conditions were correctly specified and functioning as intended.

Accordingly, the initial CFD model was configured to reproduce the results of the previous study as closely as possible. Once satisfactory agreement with the reported heat rejection was achieved, confidence in the numerical setup was established. Subsequently, an improved heat transfer formulation was introduced and implemented within the model. This approach does not alter the underlying principles of heat transfer, but rather modifies the mathematical representation used to describe the process. By maintaining an identical computational framework and boundary conditions, any differences observed in the predicted heat rejection between the two models can be directly attributed to the differences in the heat transfer formulation.

The heat transfer formulation used in previous work employs the same equations as the 1-D model (Equations (8)–(19) of this text) on a cell-by-cell basis. This required that some mathematical changes and mesh constraints needed to be applied for implementation into the CFD model. The first of these changes was the definition of the air mass flow rate, calculated from the density and the velocity as follows:

$$\dot{m}_a = \rho_{cell} v_{cell} A_{fr} \quad (44$$

By using named expressions in Fluent, the density and velocity were called to calculate the mass flow rate through the cell. A_{fr} was taken to be the frontal area of the cell. This however is not a value that can be called through named expressions and thus it needed to be set at fixed values and the mesh constrained such that the frontal area of each cell is equal to the desired value. Additionally, for the condensation heat transfer coefficient it was assumed that each cell has exactly one heat exchanger tube inside of it. This allows simplification of the equation for $\dot{m}_{ai}$ and $UdzH$ to (representing the air flow on one side of a finned tube):

 doi:10.20944/preprints202606.0307.v1

$$\dot{m}_{ai} = \frac{\dot{m}_a}{2} \tag{45}$$

$$UdzH = \frac{h_{ea} A_a}{2} \tag{46}$$

The final part of the previous formulation uses a user-defined scalar (UDS) to transport the temperature of the cell in front of the heat exchanger cell. This UDS was then used as the inlet temperature of the heat exchanger, as follows:

$$\dot{Q} = \dot{m}_a c_{pa} \epsilon \, (T_{vm} - UDS) \tag{47}$$

While the method employed in previous work was a good approximation, several improvements are suggested in this paper. The use of named expressions forces the user to call both the density and the velocity from the cell centre. This is problematic as calling the velocity at the cell centre averages the velocity stored in each of the cell faces, causing the mass flow rate used in the source term and the mass flow rate used in the Fluent solver to differ. The proposed improved method employs a user defined function (UDF) that calls on Fluent macros [29] to loop over all cell faces and determine the mass flow rate going into the cell. This directly determines the mass flow rate in the cell. Additionally, instead of using a UDS to define the heat exchanger inlet temperature, the UDF reads the temperature from the cell number and thread of the cell adjacent to the face with the largest mass flux.

Lastly, the equations for m_{ai} and $UdzH$ were modified so that more than one heat exchanger tube could be allocated to each cell:

$$\dot{m}_{ai} = \frac{\dot{m}_a}{2n_{tc}} \tag{48}$$

$$UdzH = \frac{h_{ea} A_a}{2n_{tc}} \tag{49}$$

where n_{tc} is the number of tubes in each cell. Adhering to the volumetric definition of source terms in Fluent, the resulting new source term can be defined by division with the cell volume (V_{cell}):

$$S_E = \frac{\dot{m}_a c_{pa} \epsilon \left(T_{vm} - T_{adjacent}\right)}{V_{cell}} \tag{50}$$

The exact difference between the results of two methods to model the heat transfer source term of the heat exchanger will be discussed in more detail in the results section.

The pressure drop formulation employed in previous work [16] was investigated and it was found that no significant error was induced when calling the velocity at the cell centre. This was done by modelling a straight duct with the heat exchanger inside. This formulation employs the average density across the heat exchanger and the mass flow rate through the heat exchanger. Since the temperature of the heat exchanger cells are very close to air temperature at the heat exchanger outlet in the CFD, the error in the density and velocity effectively cancel each other out, producing an extremely accurate approximation. For this reason, the same porous zone formulation was employed as that which was used in previous work. This involved setting the viscous resistance to zero and using the inertial resistance derived by Strydom et al. [16]:

$$C_n = \frac{K_{il} + K_{he} + K_{ts}}{V_{cell}} \tag{51}$$

where n is the direction normal to the heat exchangers. Note that for directions other than n, significantly larger inertial resistances are specified to ensure realistic modelling of the air directing effects of the heat exchangers.

2.2.4. Mesh Independence

To ensure that the results obtained from the CFD are independent of the mesh size, several steps were required. The first step was to establish a meshing methodology to ensure that no result is

 doi:10.20944/preprints202606.0307.v1

anomalous due to an element with poor orthogonal quality. The mesh can roughly be divided into four sections: the inside of the tower, the bottom section of the outer domain, the upper section of the outer domain and lastly the mesh bridging the tower and the outer domains.

The inside of the tower is a structured hexahedral mesh as seen in Figure 7. The key part of this section is that the heat exchanger needs to be meshed such that all elements in it have an orthogonal quality of one and with a known cell height. The reason why the cells should have an orthogonal quality of one is so that they line up perfectly with the flow direction, making calculations both more robust and more accurate. The second requirement of the heat exchanger mesh is to have a known cell height as we need the frontal area and cell height to calculate the condensation heat transfer coefficient h_c, which feeds into the overall heat transfer coefficient. Note that although this might look like heat exchange depends on the mesh, it does not, as the mass flow rate and the cell height cancel out when implemented in Equation (14).

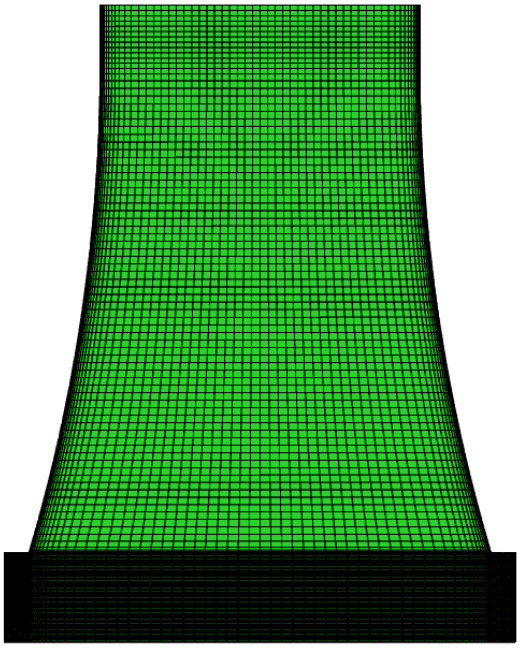

Figure 7. Tower mesh.

The outer domain, both the top and bottom sections, consist of another structured hexahedral mesh. The idea in this section was to sweep the geometry to ensure high orthogonal quality in the surroundings. The only differences between the top and bottom sections are the decreased cell heights in the bottom section to better reflect the wind profile.

Lastly, the bridging section was included as a tetrahedral mesh to bridge the mesh of the tower and the surrounding regions. An example of the mesh in this region is presented in Figures 8 and 9.

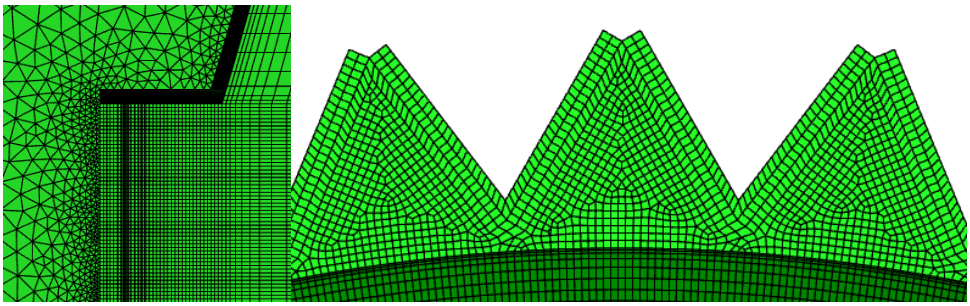

Figure 8. Heat exchanger mesh.

 doi:10.20944/preprints202606.0307.v1

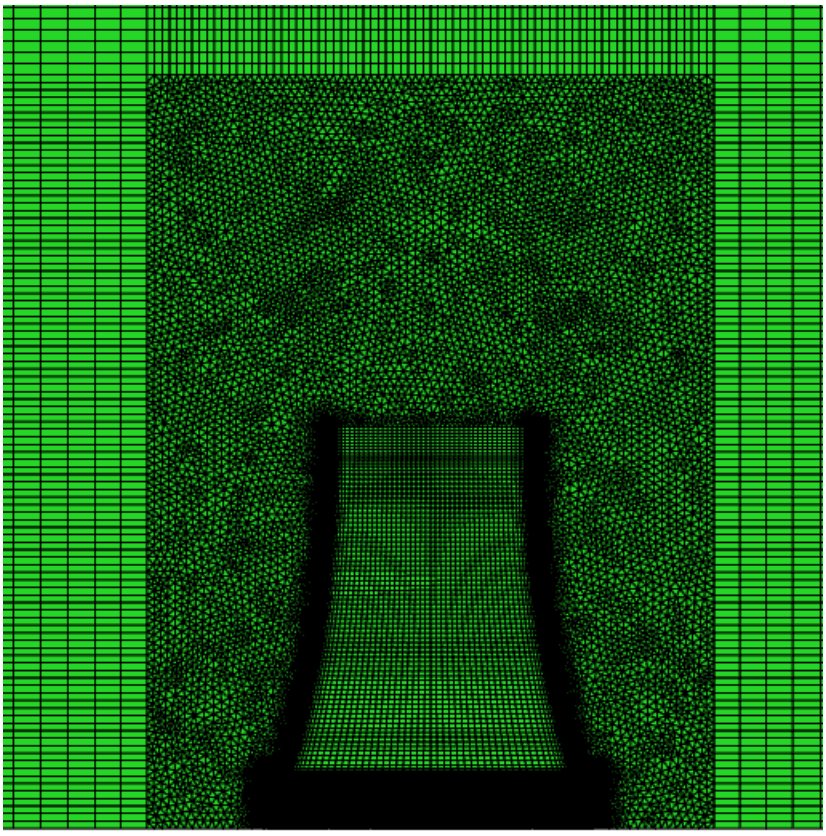

Figure 9. Surrounding mesh.

The second step of the mesh independence evaluation was to ensure that the final mesh used for simulations is sufficiently refined to capture all relevant flow phenomena. To do this a grid convergence index (GCI) study was performed. Several boundary conditions were investigated, from a zero wind condition up to a wind speed of 10 m/s (at a reference height of 10 m above ground level). A GCI study only truly confirms the mesh independence for one given set of boundary conditions, so in an ideal scenario all boundary conditions would have a GCI study associated with them. However, this is rarely feasible. Instead, a range of wind speeds were investigated as it is the main driver behind the flow patterns within the domain. This was done to find the mesh with a suitable balance between computational overhead and accuracy.

The GCI study involved uniform mesh refinement to produce a coarse, medium and fine mesh. A minimum refinement factor of 1.3 was maintained to ensure that the study does not remain within a region of apparent solution insensitivity (i.e., a false convergence region), where discretisation errors cannot be reliably assessed [30,31]. It should be noted that GCI studies were originally intended to only be used for completely structured meshes and the mesh used in this study includes an unstructured tetrahedral section, although it is relatively small. Several studies have however proven that a GCI study is still applicable to unstructured meshes [32]. The results of three GCI studies are shown in Table 5:

Table 5. GCI simulations.

Refinement	Number of Cells	Wind Speed (m/s)	Heat Rejected (MW)
Fine	22.0 million	0	76.12
Medium	9.78 million	0	76.12
Coarse	2.70 million	0	76.25
Fine	22.0 million	2.5	61.67
Medium	9.78 million	2.5	61.36
Coarse	2.70 million	2.5	60.24
Fine	22.0 million	10	38.36

 doi:10.20944/preprints202606.0307.v1

Medium	9.78 million	10	38.50
Coarse	2.70 million	10	38.90

These three studies correspond to the minimum wind speed, the most prevalent wind speed observed at Upington, and what is considered an extreme case. The first step in the GCI process is calculating the exact refinement ratio:

$$r_{21} = \frac{N_1}{N_2} \tag{52}$$

where N refers to the cell count and the subscript refers to which mesh is being referenced. Subscript 1 refers to fine, 2 to medium and 3 to coarse. The formula shown in Equation (52) calculates the refinement factor from the medium to fine mesh.

The second parameter of interest is the observed order of convergence, p, which can be calculated through an iterative approach, as follows:

$$p = \frac{1}{\ln(r_{21})}\left|\ln\left(\frac{\Phi_3 - \Phi_2}{\Phi_2 - \Phi_1}\right) + \ln\left(\frac{r_{21}^p - s}{r_{32}^p - s}\right)\right| \tag{53}$$

$$s = Sign\left(\frac{\Phi_3 - \Phi_2}{\Phi_2 - \Phi_1}\right) \tag{54}$$

where Φ refers to the parameter being investigated, which in this case refers to the heat rejection rate. With the order of convergence now calculated, the GCI value between different meshes can be obtained from:

$$\varepsilon_{21} = \left|\frac{\Phi_1 - \Phi_2}{\Phi_1}\right| \tag{55}$$

$$GCI_{21} = \frac{3\,\varepsilon_{21}}{r_{21}^p - 1} \tag{56}$$

It should be noted that the value of 3 in Equation (56) is a safety factor and it ensures that a mesh with low accuracy is not chosen inadvertently. It is recommended to keep the GCI value below 5% for individual detailed studies and below 10% for parametric studies [33]. The results derived from Equations (52)–(56) are shown in Table 6. It shows that the medium mesh performs adequately, since the refinement from coarse to medium puts the GCI value far below the threshold for all wind speeds. The medium mesh will therefore be used for all CFD simulations.

Table 6. GCI results.

Wind Speed (m/s)	GCI_{32} (%)	GCI_{21} (%)
0.0	0.160	0.0002
2.5	1.358	0.7266
10.0	1.385	0.9171

2.3. Operating Envelope Sampling Methodology

As mentioned in the introduction, in a real power plant the heat rejected by the cooling system will not reduce to very low values during nominal off-design atmospheric conditions. Instead, the steam temperature within the cooling system will increase naturally with an increase in ambient temperature or wind, to ensure that the required heat is still rejected. The rise in steam temperature would result in an associated rise in back pressure in the cooling system and at the turbine exhaust. This means that heat rejection remains nearly constant while the turbine efficiency decreases.

To generate the required training dataset for the surrogate model development will require large amounts of compute time to converge enough CFD simulations. Thus, the 1-D model was used to predict the shape of the shape of the operating envelope so that sampling can only be done from the valid operating envelope. In order to do this, the 1-D model was enhanced to include the wind effects.

 doi:10.20944/preprints202606.0307.v1

This was accomplished through combining the 1-D model with a cubic function that estimates the reduction in heat rejection due to wind. This was achieved through the following equation:

$$\dot{Q}_{new} = (1 - D)\dot{Q}_{old} \quad (57$$

where $\dot{Q}_{old}$ refers to the heat rejection predicted by the model outlined in Section 2.1.1 that only takes the ambient temperature and back pressure as input. D will be a new variable that predicts the reduction of heat rejected as a function of v_{ref}. The result of this is a 1-D model that can estimate the effects of wind on NDACC performance.

The cubic function was obtained by modelling the tower at the design back pressure and ambient temperature, while varying the wind speed in the CFD model. Once several data points were obtained a least squares approach was used to fit the cubic function as shown in Figure 10. The resultant relationship is shown in equation (58).

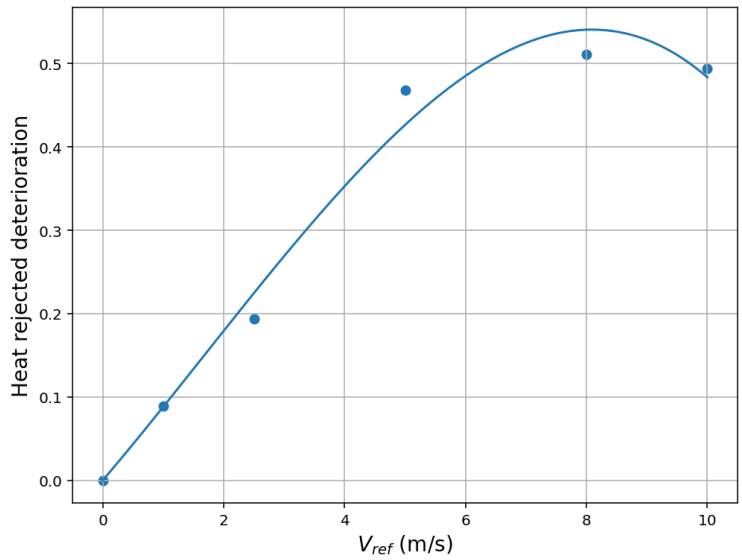

Figure 10. Effect of wind on heat rejection.

$$D = 0.085\, {v_{ref}}^3 + 0.0037\, {v_{ref}}^2 - 0.0007419\, v_{ref} \quad (58$$

Using this enhanced model an estimated back pressure can be found for a given ambient temperature and wind speed. From this a design of experiments (DOE) could be performed to select training (100) and validation (10) points that results in heat rejection values that are within +15% and −10% of the target rate of heat rejection, i.e., approximately 68–87 MW_{th}. This allows some variation around the target heat rejection rate so that the surrogate model will be able to map the response around the operating point. The envelope of operating points that defines the full range of ambient conditions encountered during an annual operating cycle of the integrated plant is shown in Figure 11.

 doi:10.20944/preprints202606.0307.v1

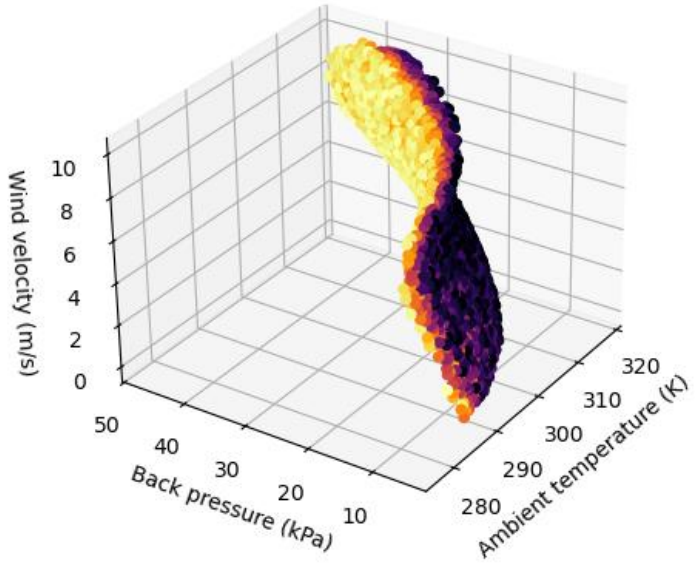

Figure 11. DOE sampling domain.

3. Results

3.1 1-D Model Results

3.1.1. Validation of the 1-D Model

Before the 1-D model could be used to determine the best-performing tower geometry, it needed to be validated. This was done in two steps. First, the model was implemented identically to how it was done by Strydom et al. [16] (including the steam-side pressure drop). For the validation case the same geometry was used as the large-scale reference tower of [16]. The main dimensions and boundary conditions for this NDACC design are shown in Table 7. It was then confirmed that the new model predicts the same heat rejected as the original model, as shown in Table 8.

Following this, the new formula set (Equations (32)–(37)) for the heat exchanger width was implemented to only allow for geometrically feasible designs. This results in a slight change in K_{ct}, as with the new heat exchanger width formulation a more accurate peripheral area, A_2, could be found. Additionally, fluid properties were determined using CoolProp [34] instead of the empirical correlations from [20]. The results from the updated model are also shown in Table 8. Analysis of the results (not shown) reveal that the implementation of the updated property correlations and K_{ct} approach have a relatively minor effect (approx. 0.5%), while the change in heat exchanger width is the main driver of the observed difference in predicted heat rejection rate (approx. 9%).

Table 7. Validation geometry and boundary conditions.

Parameter	Value
Total tower height	165 m
Heat exchanger height	16.5 m
Tower base diameter	165 m
Tower outlet diameter	82.5 m
Back pressure	12.35 kPa
Ambient temperature	293.15 K

Table 8. 1-D model NDACC performance predictions.

1-D Model	Heat Rejected (MW)
Strydom et al. [16]	905.71
Current model ([16] formulation)	905.71
Current model (updated formulation)	820.62

 doi:10.20944/preprints202606.0307.v1

3.1.2. Best-Performing NDACC Configuration for CSP Application

After validation of the 1-D model for the large-scale reference NDACC, it was used to re-size the system according to the design point parameters for the 50 MWe CSP application, while aiming to find most cost-effective geometric configuration at this scale. The exhaustive search method described in section 2.1.2 was used to populate the design space as shown in Figure 12. The figure shows the geometric ratios on the x, y and z axis, and the normalized total material cost to construct each tower configuration determines the colour of the datapoint. Lighter colours correspond to more expensive tower designs and darker colours are the less expensive designs. Additionally, the geometry of the best-performing tower was included in Table 9.

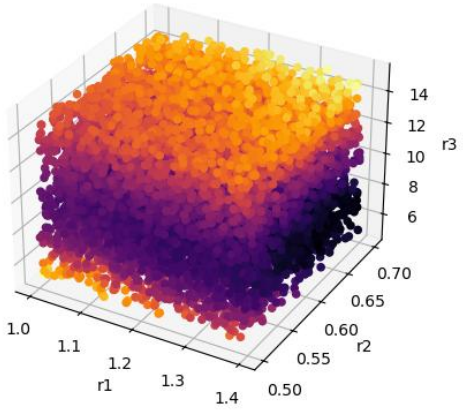

$$r_1 = \frac{H_5}{d_3}$$

$$r_2 = \frac{d_5}{d_3}$$

$$r_3 = \frac{d_5}{H_4}$$

Figure 12. Best-performing ratios.

Table 9. Best-performing NDACC geometry.

Parameter	Value
Total tower height	78.97 m
Heat exchanger height	11.15 m
Tower base diameter	56.87 m
Tower outlet diameter	39.37 m
r_1	1.39
r_2	0.69
r_3	5.10

Some interesting observations can be made about the tower cost from the figure. First, it is noticeable that there is a banded region of lower tower cost designs. This occurs due to a balance that needs to be maintained between the heat exchanger surface area and the draft potential of the tower. A shorter tower needs a larger surface area of heat exchangers to deliver the same heat transfer rate, since the lower the tower height, the lower the draft potential. This lower draft potential means the mass flow rate of air through the tower will be lower and thus to achieve the same heat transfer rate the heat transfer area needs to increase. The inverse is also true, meaning a tower with a wide base will have a larger heat transfer area and thus a lower draft potential is necessary to achieve the same heat rejection.

From this the results can be interpreted as follows: The first geometric ratio r_1 should be maximized. This means a narrow tower with a small base. The narrow design allows the tower to be built taller for the same cost leading to an increase in draft potential. The increased draft potential can compensate for a decrease in heat exchanger surface area when minimizing the tower size. This is beneficial as the heat exchanger cost is the main driver to the overall tower cost. The second geometric ratio r_2 needs to be maximized as well. This is less intuitive than the first, but a tower with a similar base and outlet diameter has a lower pressure loss through the tower and thus a greater draft potential. Lastly, the third geometric ratio r_3 needs to be selected based on the other ratios. This ratio is inversely proportional to the height of the heat exchangers. This means that when r_3 is

 doi:10.20944/preprints202606.0307.v1

decreased the heat exchange surface area increases. Note that although this changes the heat exchanger height it does not change the total tower height, so it has a limited effect on the draft potential. This means that for large r_1 and r_2 values a smaller r_3 value should be selected, as with large r_1 and r_2 values the draft potential is already high, allowing the tower to be decreased in size. The small r_3 value, meaning larger (taller) heat exchangers, offsets this downscaling effect, allowing for the same heat rejection with a smaller tower. For small r_1 values the heat exchangers are wider and thus decreasing r_3 (therefore increasing the heat exchanger height) has a smaller effect since beyond a certain heat exchange surface area the increase in air mass flow rate is not as significant.

3.2. CFD results

3.2.1. Validation of the CFD Model

As for the 1-D model, the CFD model first needed to be validated against previous results to ensure the reliability of the current model. This was done through two methods: First, the predicted heat rejection rate from the CFD was directly compared to the validated CFD results of Strydom et al. [16]. In Table 10 the results of both heat exchanger models described in Section 2.2.3 are shown. To better visualize the difference between the models a step-by-step approach was taken to implement the new model. First the CFD model was recreated exactly as in previous work and that yielded the second row. Then the new method was employed to retrieve the inlet temperature of the heat exchanger, and this yielded the third row. Finally, the mass flow rate was calculated using Fluent macros instead of Equation (44), coupling the heat exchanger source term directly to the continuity equation. This yielded the final row in Table 10.

Table 10. CFD validation results.

Method	Temperature	Mass Flux	Heat Rejected (MW)
Strydom et al. [16]	UDS	Named Expression	927.51
Current work	UDS	Named Expression	926.64
Current work	UDF	Named Expression	920.93
Current work	UDF	UDF	956.72

The second part of the validation process involved verifying that the simulation reproduces the key flow phenomena reported in previous studies. The first of these is the flow separation point at the tower inlet, caused by downward airflow from above the clapboard into the heat exchangers. A visual comparison of these flow features between the current and previous study clearly shows the agreement, as presented in Figure 13.

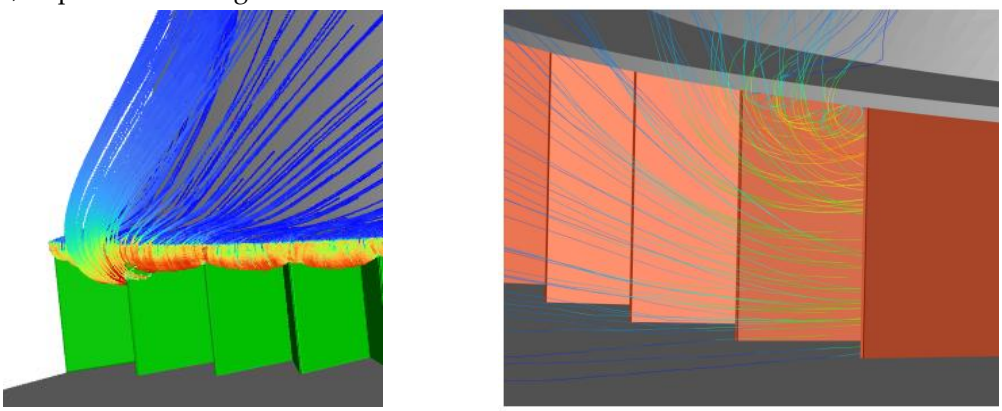

(**a**) (**b**)

Figure 13. Recirculation phenomenon: (**a**) Current work; (**b**) Strydom et al. [16].

The second verified flow phenomenon consists of localised hotspots on the heat exchanger inlet faces, which arise due to a recirculation zone forming upstream of the heat exchangers (due to the previously noted flow separation). A comparison of the contour plots in Figure 14 clearly

 doi:10.20944/preprints202606.0307.v1

demonstrates similar trends to prior work, while also confirming the capability of the current CFD model to accurately model localised heat transfer behaviour.

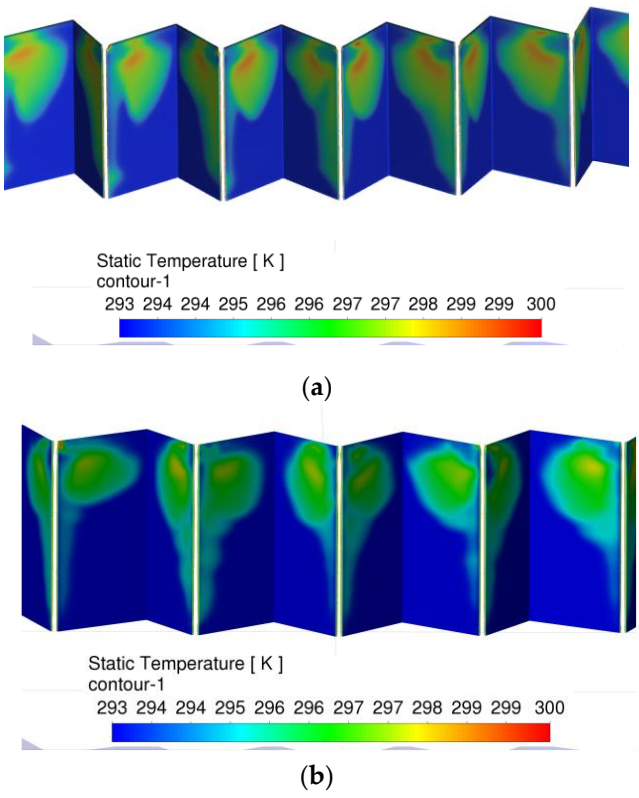

Figure 14. Localised heat exchanger hot spots phenomenon: (**a**) Current work; (**b**) Strydom et al. [16].

3.2.2. Finalizing NDACC Sizing for CSP application

To verify that the NDACC in the CFD model can dissipate the required 75 MW_{th} at the design point parameters for the CSP application, an iterative sizing approach was adopted (as discussed in section 2.2). First, a CFD simulation was performed using the dimensions of the best-performing NDACC configuration, as obtained from the 1-D model. As noted before, due to the intrinsic differences and simplifications of the 1-D vs 3-D CFD model, the CFD results indicated a slightly lower heat rejection rate compared to the 1-D prediction. The NDACC size of the CFD model was subsequently increased to achieve the desired rate of heat rejection. It should be noted that during the scaling process the geometric ratios change slightly as the heat exchanger dimensions are discrete rather than continuous. Two scaling iterations were required to achieve a conservative heat rejection rate of 76 MW_{th}, using an 80 m tower height. The results are shown in Table 11.

Table 11. Iterative NDACC sizing in CFD model.

H_5 (m)	H_4 (m)	d_3 (m)	d_5 (m)	W_b (m)	Heat Rejected (MW)
79	11.25	56.90	39.40	3.484	73.89
82	11.50	59.00	40.90	3.618	80.11
80	11.25	58.00	40.15	3.551	76.10

3.2.3. Impact of Wind on Performance

The CFD simulation results for the best-performing NDACC configuration clearly shows the degradation of system performance under high crosswind conditions. This is due to two reasons. The first is a decrease in the effective tower outlet area, which effectively chokes the air mass flow rate through the system. At high wind speeds, the hot air plume at the tower exit is flattened, which interferes with the air flow rising through the tower. The impact of wind is illustrated through a

 doi:10.20944/preprints202606.0307.v1

comparison between Figure 15 and 16. Figure 15 shows the NDACC operating with an ITD of 17.5 K under no-wind conditions, while Figure 16 depicts the NDACC operating with the same 17.5 K ITD, but under a 10 m/s crosswind. The hot air plume rises vertically in Figure 15, while the flattened plume is shown clearly in Figure 16.

The air temperatures within the tower are also a few degrees cooler under crosswind compared to no-wind conditions. With lower mass flow through the system, heat exchanger effectiveness reduces, causing lower heat exchanger outlet air temperatures. This will service to further lower the draft driving potential.

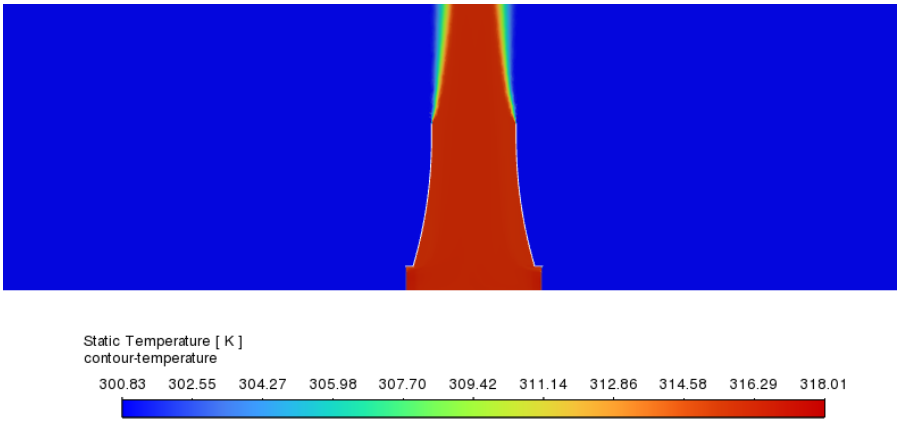

Figure 15. Side profile static temperature contour plot of NDACC under no-wind conditions.

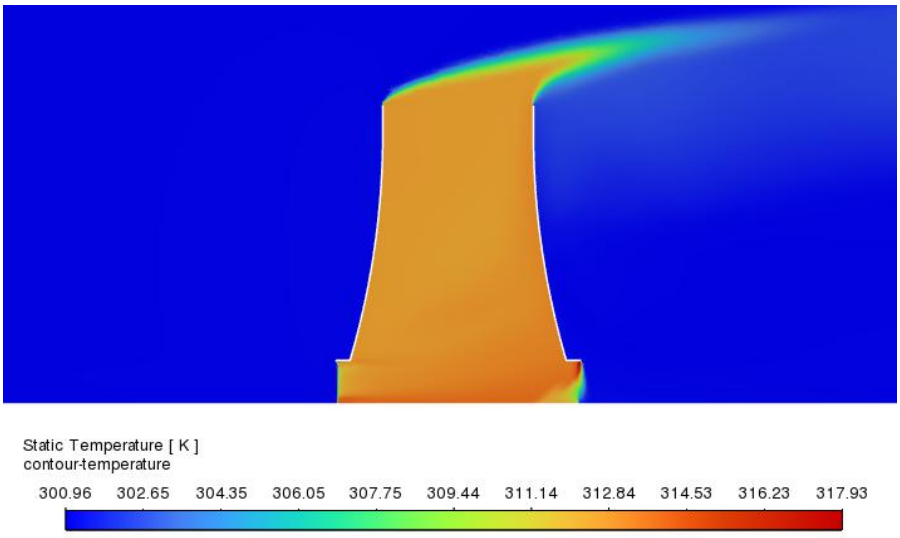

Figure 16. Side profile static temperature contour plot of NDACC under 10 m/s crosswind.

The second phenomenon that causes the decrease in system performance is air recirculation and reverse flow at the heat exchangers. Under calm conditions there are clear air temperature differences between the inside and outside of the tower, as no recirculation occurs and the draft is functioning normally (see Figure 17). At high wind speeds however, air accelerates around the cooling tower, especially in the middle sectors and leeward side (see Figure 18). Recirculation, reverse flow and air flow separation effects near the heat exchangers all contribute to reduced effective air flow through the system, which are again detrimental to the draft driving potential.

 doi:10.20944/preprints202606.0307.v1

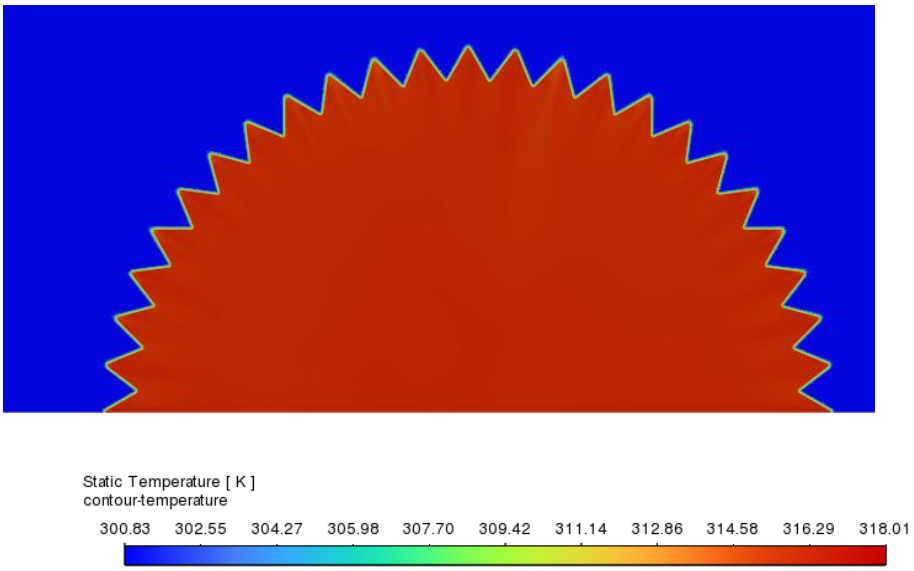

Figure 17. Cross-section static temperature contour plot of NDACC under no-wind conditions .

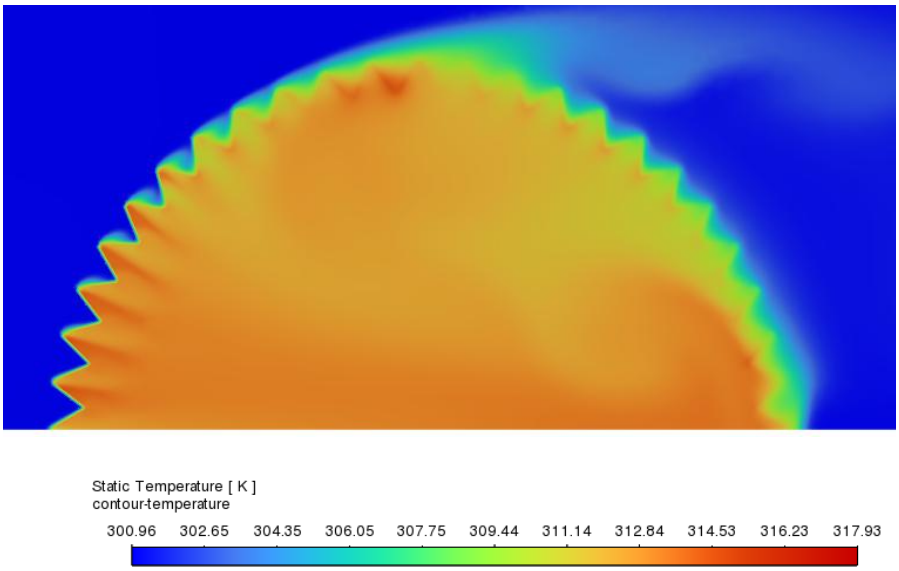

Figure 18. Cross-section static temperature contour plot of NDACC under 10 m/s crosswind .

3.3. Performance Envelope Analysis

In order to demonstrate the operating envelope sampling methodology described in Section 2.3, a sample of 10 operating points were drawn via LHS from the valid operating envelope shown in Figure 11. The performance of each of these samples was determined via the validated CFD model and the results are presented in Figure 19.

 doi:10.20944/preprints202606.0307.v1

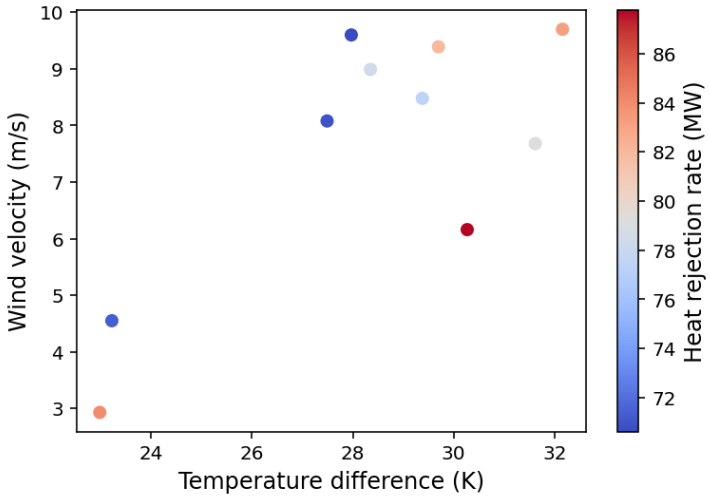

Figure 19. Sample dataset results.

In this figure the temperature difference between the mean steam temperature and the ambient air temperature is shown on the x-axis and the wind velocity v_{ref} is shown on the y-axis. The resultant rate of heat rejection is represented by the colours of the symbols according to the scale shown alongside.

The results show that the sampling methodology ensured that all of the operating points lie within the desired range of heat rejection rate, i.e., 68–87 MW_{th}. The resultant operating envelope also demonstrates that at low wind speeds a small temperature difference will result since a high rate of heat rejection can be achieved despite the small temperature difference between the steam and the air. Inversely, at high wind speeds the degradation in performance will result in a large temperature difference in order to maintain the desired heat rejection rate.

These results provide confidence in the sampling methodology to eventually generate the larger training dataset that will be used in further work to train and deploy the surrogate model.

4. Conclusion

The validated and modified 1-D model was successful at finding the dimensions of a best-performing NDACC configuration for a 50 MWe CSP application. This was achieved by incorporating a simplified cost model and minimizing material costs by performing an exhaustive search within the permissible ranges of geometric ratios. This process showed that the geometric ratios produce a less expensive cooling tower if the ratio favours the draft potential rather than the surface area of the heat exchanger. The best-performing tower was shown to be a narrow tower with similar base and outlet diameters and tall heat exchangers. The slender configuration reduces concrete usage, while similar outlet and base diameters limit pressure losses as the air rises. Taller heat exchangers increase the heat transfer area, allowing the tower to be scaled down until the reduction in draft potential offsets the gain in heat transfer.

To ensure the accuracy of the CFD model it was first validated against previous work, and multiple GCI studies were performed to ensure mesh independence. Additionally, an iterative process was used to determine the final NDACC dimensions for the CFD model, as the 1-D model slightly overpredicts the heat rejection. Note that the best-performing geometric ratios were kept as consistent as possible throughout this iteration process. Using this final geometry an investigation was conducted into the effects of varying the ambient temperature, back pressure and the wind velocity. From these results it was observed that wind decreases the predicted heat rejection rate up until a wind speed of roughly 8 m/s, at which point the heat rejection makes a slight recovery as wind speed increases. Additionally, simulation results show that to maintain the required 75 MW_{th} of heat rejection necessary for the CSP power plant, the back pressure, and thus steam temperature, would need to increase to offset reduced NDACC performance under increased ambient temperature and wind.

 doi:10.20944/preprints202606.0307.v1

After the CFD was validated and the wind profile was established, the 1-D model was enhanced to incorporate the deterioration effect of wind and then used to estimate the shape of the valid operating envelope of the chosen design. This allows for a more precise sampling that should decrease the number of datapoints required to train the surrogate model by focusing them around the valid operating point that captures only the relevant operating points.

For future work the proposed sampling methodology together with the CFD model will be used to generate a training dataset which will be employed to train a reduced order surrogate model that can provide good results within very quick computing times. Integrating this reduced order model with a CSP plant model will allow annual performance studies based on hourly predictions to be conducted within reasonable computer running times.

Author Contributions: Conceptualization, J.P.P. and P.G.R.; methodology, J.P.P., P.G.R. and T.N.; software, T.N.; formal analysis, T.N.; writing—original draft preparation, T.N.; writing—review and editing, J.P.P. and P.G.R.; visualization, T.N. All authors have read and agreed to the published version of the manuscript.

Funding: This research received no external funding.

Data Availability Statement: The raw data supporting the conclusions of this article can be made available by the authors on request.

Acknowledgments: The authors would like to acknowledge the solar thermal energy research group (STERG) at the Mechanical and Mechatronic Engineering Department at Stellenbosch University, who provided funding to present this work at the Africomp 7 conference. Furthermore, the authors acknowledge the Centre for High Performance Computing (CHPC), South Africa, for providing computational resources to this research project.

Conflicts of Interest: The authors declare no conflicts of interest.

Abbreviations

The following abbreviations are used in this manuscript:

1-D	One-dimensional
3-D	Three-dimensional
ACC	Air-cooled condenser
AI	Artificial intelligence
CFD	Computational fluid dynamics
CHPC	Centre for high performance computing
CSP	Concentrated solar power
DOE	Design of experiments
GCI	Grid convergence index
ITD	Initial temperature difference
LHS	Latin hypercube sampling or left-hand side
NDACC	Natural draft air-cooled condenser
NDDDCS	Natural draft direct dry cooling system
NTU	Number of transfer units
PISO	Pressure-implicit with splitting operators
PRESTO	Pressure staggering option
RHS	Right-hand side
SIMPLE	Semi implicit method for pressure linked equations
SIMPLEC	Semi implicit method for pressure linked equations consistent
STERG	Solar thermal energy research group
UDF	User defined function
UDS	User defined scalar

References

1. I. E. Agency, "Energy and AI," 2025. [Online]. Available: https://www.iea.org/reports/energy-and-ai
2. "P0302 - Mid-year population estimates, 2025," Department of Statistics of South Africa, South Africa, 2025. [Online]. Available: https://www.statssa.gov.za/?PPN=P0302&page_id=1854

 doi:10.20944/preprints202606.0307.v1

3. N. Fulghum, W. Suarez, K. Altieri, and K. Rangelova, "Global Electricity Review 2026," Ember, 2026. [Online]. Available: https://ember-energy.org/latest-insights/global-electricity-review-2026/
4. D. Ciolkosz, "SASRAD: An hourly-timestep solar radiation database for South Africa," (in en), *Journal of Energy in Southern Africa*, vol. 20, no. 1, pp. 25-34, %02/%01 2009, doi: 10.17159/2413-3051/2009/v20i1a3299.
5. I. H. Njoku and O. E. Diemuodeke, "Techno-economic comparison of wet and dry cooling systems for combined cycle power plants in different climatic zones," *Energy Conversion and Management*, vol. 227, p. 113610, 2021/01/01/ 2021, doi: https://doi.org/10.1016/j.enconman.2020.113610.
6. R. Nazar, "Water-reduction potential of air-cooled condensers in coal power plants in India and anticipated trade-offs," *Applied Water Science*, vol. 10, no. 7, p. 162, 2020/06/12 2020, doi: 10.1007/s13201-020-01246-8.
7. S. Duniam, I. Jahn, K. Hooman, Y. Lu, and A. Veeraragavan, "Comparison of direct and indirect natural draft dry cooling tower cooling of the sCO2 Brayton cycle for concentrated solar power plants," *Applied Thermal Engineering*, vol. 130, pp. 1070-1080, 2018/02/05/ 2018, doi: https://doi.org/10.1016/j.applthermaleng.2017.10.169.
8. F. S. Marincowitz, M. T. F. Owen, and J. Muiyser, "The Effect of Windscreens and Walkways on Air-Cooled Condenser Performance and Fan Blade Dynamic Loading," *Journal of Engineering for Gas Turbines and Power*, vol. 143, no. 10, 2021, doi: 10.1115/1.4051640.
9. K. Duvenhage and D. G. Kröger, "The influence of wind on the performance of forced draught air-cooled heat exchangers," *Journal of Wind Engineering and Industrial Aerodynamics*, vol. 62, no. 2, pp. 259-277, 1996/09/01/ 1996, doi: https://doi.org/10.1016/S0167-6105(96)00082-7.
10. D. L. Louw, "Performance comparison of forced draft and induced draft air-cooled condensers under adverse Crosswind Conditions.," PhD thesis, Department of Mechanical and Mechatronic Engineering, Stellenbosch University, Stellenbosch, 2021.
11. R. A. Kheneslu, A. Jahangiri, and M. Ameri, "Interaction effects of natural draft dry cooling tower (NDDCT) performance and 4E (energy, exergy, economic and environmental) analysis of steam power plant under different climatic conditions," *Sustainable Energy Technologies and Assessments*, vol. 37, p. 100599, 2020/02/01/ 2020, doi: https://doi.org/10.1016/j.seta.2019.100599.
12. Y. Kong, W. Wang, X. Huang, L. Yang, and X. Du, "Thermo-flow performances of natural draft direct dry cooling system at ambient winds," *International Journal of Heat and Mass Transfer*, vol. 116, pp. 173-184, 2018/01/01/ 2018, doi: https://doi.org/10.1016/j.ijheatmasstransfer.2017.09.020.
13. Y. Kong, W. Wang, X. Huang, L. Yang, X. Du, and Y. Yang, "Combined air-cooled condenser layout with in line configured finned tube bundles to improve cooling performance," *Applied Thermal Engineering*, vol. 154, pp. 505-518, 2019, doi: 10.1016/j.applthermaleng.2019.03.099.
14. Y. Kong, W. Wang, X. Huang, L. Yang, and X. Du, "Annularly arranged air-cooled condenser to improve cooling efficiency of natural draft direct dry cooling system," *International Journal of Heat and Mass Transfer*, vol. 118, pp. 587-601, 2018/03/01/ 2018, doi: https://doi.org/10.1016/j.ijheatmasstransfer.2017.11.031.
15. Y. Kong, W. Wang, X. Huang, L. Yang, X. Du, and Y. Yang, "Wind leading to improve cooling performance of natural draft air-cooled condenser," *Applied Thermal Engineering*, vol. 136, pp. 63-83, 2018, doi: 10.1016/j.applthermaleng.2018.02.100.
16. W. Strydom, "Natural Draft Direct Dry Cooling System Performance at Various Application Scales Under Steady and Transient Conditions," PhD thesis, Department of Mechanical and Mechatronic Engineering, Stellenbosch University, Stellenbosch, 2024.
17. W. Strydom, J. Pretorius, and J. Hoffmann, "Natural Draft Direct Dry Cooling System scaling for diverse applications," presented at the International conference on heat transfer, fluid mechanics and thermodynamics, Virtual Conference, 2022.
18. W. Strydom, J. Pretorius, and J. Hoffmann, "Sensitivity Analysis on the Performance of a Natural Draft Direct Dry Cooling System for a 50 MWe CSP Application," presented at the Proceedings of the 8th World Congress on Momentum, Heat and Mass Transfer, 2023.
19. W. Strydom, J. Pretorius, and J. Hoffmann, "Natural draft direct dry cooling system performance at various application scales under windless and windy conditions," *Applied Thermal Engineering*, vol. 248, p. 123181, 2024/07/01/ 2024, doi: https://doi.org/10.1016/j.applthermaleng.2024.123181.
20. D. G. Kröger, Air-cooled Heat Exchangers and Cooling Towers. 1998.

 doi:10.20944/preprints202606.0307.v1

21. K. M.-L. v. Rooyen and J. Fick, "The effect of condenser backpressure on station thermal efficiency: Grootvlei Power Station as a case study," Development and Management Engineering, North-West University, Potchefstroom, South Africa, 2014. [Online]. Available: https://repository.nwu.ac.za/items/545286c5-7af0-443e-a0a3-e8cbddd7862a
22. R. A. Haffejee and R. Laubscher, "Application of machine learning to develop a real-time air-cooled condenser monitoring platform using thermofluid simulation data," *Energy and AI,* vol. 3, 2021, doi: 10.1016/j.egyai.2021.100048.
23. J. Singh, "Ranking South African provinces on the basis of MERRA 2D surface incident shortwave flux," (in en), *Journal of Energy in Southern Africa,* vol. 27, no. 3, pp. 50-57, %09/%23 2016, doi: 10.17159/2413-3051/2016/v27i3a1555.
24. C. H. v. Niekerk, "Design and analysis of a natural draft direct dry cooling system for a supercritical carbon dioxide power cycle for CSP application," Master of Mechanical Engineering, Department of Mechanical and Mechatronic Engineering, Stellenbosch University, Stellenbosch, 2026. [Online]. Available: https://scholar.sun.ac.za/items/330a3b9d-ef89-4c91-a692-2f17d5a109c5
25. H. K. Versteeg and W. Malalasekera, An Introduction to Computational Fluid Dynamics: The Finite Volume Method, 2nd ed. 2007.
26. F. Menter, "Menter, F.: Two-Equation Eddy-Viscosity Transport Turbulence Model for Engineering Applications. AIAA Journal 32(8), 1598-1605," *AIAA Journal,* vol. 32, 09/01 1994, doi: 10.2514/3.12149.
27. F. Menter and T. Esch, "ELEMENTS OF INDUSTRIAL HEAT TRANSFER PREDICTIONS," presented at the BRAZILIAN CONGRESS OF MECHANICAL ENGINEERING, 2001. [Online]. Available: https://www.researchgate.net/file.PostFileLoader.html?id=58500561b0366d121d756004&assetKey=AS:438841040478208@1481639265395.
28. D. S. Jang, R. Jetli, and S. Acharya, "COMPARISON OF THE PISO, SIMPLER, AND SIMPLEC ALGORITHMS FOR THE TREATMENT OF THE PRESSURE-VELOCITY COUPLING IN STEADY FLOW PROBLEMS," *Numerical Heat Transfer,* vol. 10, no. 3, pp. 209-228, 1986/09/01 1986, doi: 10.1080/10407788608913517.
29. "ANSYS FLUENT 12.0/12.1 Documentation." ANSYS FLUENT. https://www.afs.enea.it/project/neptunius/docs/fluent/index.htm (accessed.
30. P. J. Roache, "Perspective: A Method for Uniform Reporting of Grid Refinement Studies," *Journal of Fluids Engineering,* vol. 116, no. 3, pp. 405-413, 1994, doi: 10.1115/1.2910291.
31. "Procedure for Estimation and Reporting of Uncertainty Due to Discretization in CFD Applications," *Journal of Fluids Engineering,* vol. 130, no. 7, 2008, doi: 10.1115/1.2960953.
32. N. Baker, G. Kelly, and P. D. O'Sullivan, "A grid convergence index study of mesh style effect on the accuracy of the numerical results for an indoor airflow profile," *International Journal of Ventilation,* vol. 19, no. 4, pp. 300-314, 2020/10/01 2020, doi: 10.1080/14733315.2019.1667558.
33. T.-R. Teschner, "How to manage uncertainty in CFD: the grid convergence index," in *CFD.University*, ed, 2025.
34. I. H. Bell, J. Wronski, S. Quoilin, and V. Lemort, "Pure and Pseudo-pure Fluid Thermophysical Property Evaluation and the Open-Source Thermophysical Property Library CoolProp," *Industrial & Engineering Chemistry Research,* vol. 53, no. 6, pp. 2498-2508, 2014/02/12 2014, doi: 10.1021/ie4033999.